Isophotonic reactor for the precise determination of quantum yields in gas, liquid, and multi-phase photoreactions

Paul Kant [a,*], Laura L. Trinkies [a], Nils Gensior [a], Domenik Fischer [a], Michael Rubin [a,b], Geoffrey Alan Ozin [c], Roland Dittmeyer [a,b]

[a] *Institute for Micro Process Engineering (IMVT), Karlsruhe Institute of Technology (KIT), Hermann-von-Helmholtz-Platz 1, 76344 Eggenstein-Leopoldshafen, Germany*
[b] *Institute of Catalysis Research and Technology (IKFT), Karlsruhe Institute of Technology (KIT), Hermann-von-Helmholtz-Platz 1, 76344 Eggenstein-Leopoldshafen, Germany*
[c] *Department of Chemistry, University of Toronto (UofT), 80 St. George Street, Toronto M5S 3H6, Canada*

A B S T R A C T

Photocatalytic processes are an emerging field with a multitude of potential applications ranging from waste and wastewater treatment over fine chemical production to artificial photosynthesis. Knowing the quantum yield in a photoreaction is thereby essential to both, the selection of suitable photocatalysts and the design of optimized photoreactors. Nevertheless, the precise determination of quantum yields as function of the operating conditions is still a challenge without standardized and reliable procedures and apparatuses. Herein a novel approach for the accurate determination of quantum yields based on a tailored, 3D-printable photoreactor and 3D optical modelling is reported. Besides wavelength, temperature, and reactant concentration control, the unique optical design of an isophotonic reactor enables the control of the local volumetric rate of photon absorption to be homogeneous throughout the reaction volume. The validity of the approach is demonstrated by determining the quantum yield of the standard potassium ferrioxalate actinometer. Further, the adaptability to any gas, liquid, or multi-phase photoreaction is outlined by showcasing the ability of the approach with an exemplary aerogel-supported titania-based methanol reforming photocatalyst. The revealed subtlety and complex nature of the quantum yield in the methanol reforming system highlights the need for meticulous analysis and standardization of the determination of quantum yields and thereby underlines the value of the proposed approach. Software tools and print files provided alongside the publication facilitate adaptation and further development of the approach by researchers in the field.

$$\eta = \frac{\#\,of\ production\ events}{\#\,of\ incident\ photons\ in\ specific\ band} \tag{1}$$

1. Introduction

1.1. Motivation

Photocatalytic processes are an emerging field with growing interest and a multitude of potential applications ranging from waste [1] and wastewater treatment [2,3] over fine chemical production [4] to artificial photosynthesis [5,6]. The economic viability of most photocatalytic processes stands and falls with the achieved photocatalytic efficiency [6–9], the efficiency metric of the *process* relating the number of production events to the number of incident photons in a specific optical band, Eq. (1) [10]. This especially holds for solar driven processes.

The overall photocatalytic efficiency of a photocatalytic process is thereby predominantly shaped by its three essential elements: the photocatalyst, the photoreactor and the light source employed [8,9]. The light source may be regarded as part of the photoreactor as is the case in the present work. Both, the selection of suitable photocatalysts and the design of optimal photoreactors depend on the knowledge of the quantum yield, the efficiency metric of the *photocatalyst* relating the number of production events to the number of photons absorbed by the catalyst at a specific wavelength, Eq. (2) [10]. Of utmost importance for the design of photoreactors is the dependency of the quantum yield on operating conditions such as temperature (T), reactants' concentration (c), wavelength (λ), and local volumetric rate of photon absorption ($L^a_{p,\lambda}$), meaning the number of photons at a specific wavelength absorbed per

* Corresponding author.
  E-mail address: paul.kant@kit.edu (P. Kant).

Nomenclature

α	angle of incidence, rad	I_0	incoming ray intensity, W
β	angle of refraction, rad	I_{LED}	LED drive current, A
η	photocatalytic efficiency	$L_{p,\lambda}^a$	local volumetric rate of photon absorption, einstein m^{-3} s^{-1}
$\eta_{T,\lambda}$	spectral radiation transport efficiency		
Θ	polar angle, rad	n	ray direction normal vector
λ	Wavelength, nm	n_1	refractive index originating medium
ν	photon frequency, Hz	n_2	refractive index entering medium
σ_a	absorption coefficient, m^{-1}	n_{e^-,H_2}	number of transferred electrons per hydrogen molecule
σ_s	scattering coefficient, m^{-1}	$\dot{N}_{N_2}$	nitrogen feed rate, mol/s
τ	space time, h	q	emitted total flux, W
φ	azimuth angle, rad	q_λ	emitted spectral flux, W/nm
Φ	quantum yield	q_p	emitted total photon flux, einstein s^{-1}
$\overline{\Phi}$	average quantum yield (in considered narrow band)	$q_{p,\lambda}$	emitted spectral photon flux, einstein s^{-1} nm^{-1}
$\overline{\Phi}_{estimated}$	estimated average quantum yield	r	goniometer arm radius, m
$\overline{\Phi}_{H_2}$	average quantum yield of hydrogen production	R	reflectivity
A	aperture area, m^2	$\dot{r}_{Fe^{II+}}$	iron-(II)-reaction rate, mol m^{-3} s^{-1}
c	species concentration, mol m^{-3}	R	reflectivity
$c_{Fe^{2+}}$	iron-(II)-concentration, mol m^{-3}	T	Temperature, $°$ C
h	Plank constant, J s	V	reaction volume, m^3
I	ray intensity, W	y_{H_2}	hydrogen molar fraction in reactor effluent
		y_{N_2}	nitrogen molar fraction in reactor effluent

unit time and unit volume. Still, this detailed information on quantum yields is seldomly reported.

$$\Phi = \frac{\#\,of\ production\ events}{\#\,of\ absorbed\ photons\ at\ specific\ wavelength} = f\left(T, c, \lambda, L_{p,\lambda}^a\right) \qquad (2)$$

On a side note, the definition of the quantum yield can be extended according to the IUPAC recommendation for terms in photocatalysis to differentiate between an integral and a differential quantum yield [10]. Whereas the integral quantum yield relates time-integral values, the differential quantum yield relates rates (reaction rates and photon absorption rates) to each other. In systems in which, for instance, a distinct dependency of the quantum yield on the reactant concentration is observed, integral and differential quantum yield differ from each other.

Most literature works on quantum yields report apparent quantum yields that are derived from experiments that are conducted under conditions in which the number of incident photons can be assumed to equal the number of photons absorbed by the photocatalyst, see for instance [11–14]. Typical setups are simple irradiated glass vessels or reaction chambers with windows like described in [14]. Noteworthy, photon losses through scattering events in the photocatalyst bed are not considered in these approaches. The latter entails a systematic underestimation of the quantum yield of the examined photocatalysts. Black body photoreactors, like introduced for instance in [15], address this issue by placing the light source in a cavity surrounded by the employed photocatalyst. This setup ensures full photon absorption even in highly scattering photocatalysts by guaranteeing that scattered photons are redirected towards the photocatalyst. Importantly, in both approaches, the layer thickness of the catalyst must be chosen sufficiently high to guarantee that there are no significant transmissive losses. Such systems, however, inherently depict high gradients in the field of the local volumetric rate of photon absorption or process intensity respectively. A particular lack of knowledge is therefore present for the dependency of the quantum yield on the local volumetric rate of photon absorption. For the experimental examination of this dependency, photoreactors with zero or small gradients in the field of the local volumetric rate of photon absorption – isophotonic photoreactors – are highly desirable. This is in analogy to isothermal reactors that are highly desirable if not mandatory for the experimental examination of the temperature dependency of thermochemical reactions.

Within the contribution presented herein, we therefore propose a novel approach for the reliable determination of quantum yields in gas, liquid, and multi-phase photocatalytic reactions under isophotonic conditions. The 3D-printable photoreactor we employ allows for the control of temperature, reactants' concentration, wavelength, and the local volumetric rate of photon absorption. The detailed report includes the validation of our method via the determination of the quantum yield of the standard potassium ferrioxalate actinometer and comparison of the obtained data to literature data. Further, results of an exemplary application of our approach to a titania-based methanol reforming photocatalyst delineates the subtle and complex nature that quantum yields present. The concluding discussion sets into perspective the influences of the interdependencies of the quantum yield and operating conditions onto high efficiency production photoreactor design and thereby highlights the value of the proposed approach.

1.2. Description of the approach

Quantum yield measurements require experimental access to the number of events – in photoredox reactions the number of transferred electrons – and experimental or simulative access to the number of photons absorbed by the photocatalyst at a specific wavelength, Eq. (2) [10]. Noteworthy in case of a heterogeneously catalysed photoreaction, 'photocatalyst' refers to the particulate photocatalyst bed. In case of a homogenous photoreaction – with or without dissolved photocatalyst – 'photocatalyst' refers to the mixture of reactants.

In most cases, the number of events can easily be derived experimentally by determining the number of product molecules via standard analytical methods, for instance via UV–vis spectroscopy or liquid or gas chromatography. The major challenge arises from the determination of the number of absorbed photons at a specific wavelength [10]. This holds especially in heterogeneous photocatalysis where photon scattering by the photocatalyst bed significantly influences the radiation transport problem in the system [10]. In the introduced approach the number of photons absorbed by the photocatalyst is derived via spectrally resolved 3D optical simulations conducted using a MATLAB®-based implementation of a Monte Carlo ray tracing (MCRT) method. For details on the method and implementation, see Appendix A, including Fig. A.1 which shows an overview of the implementation's code in a
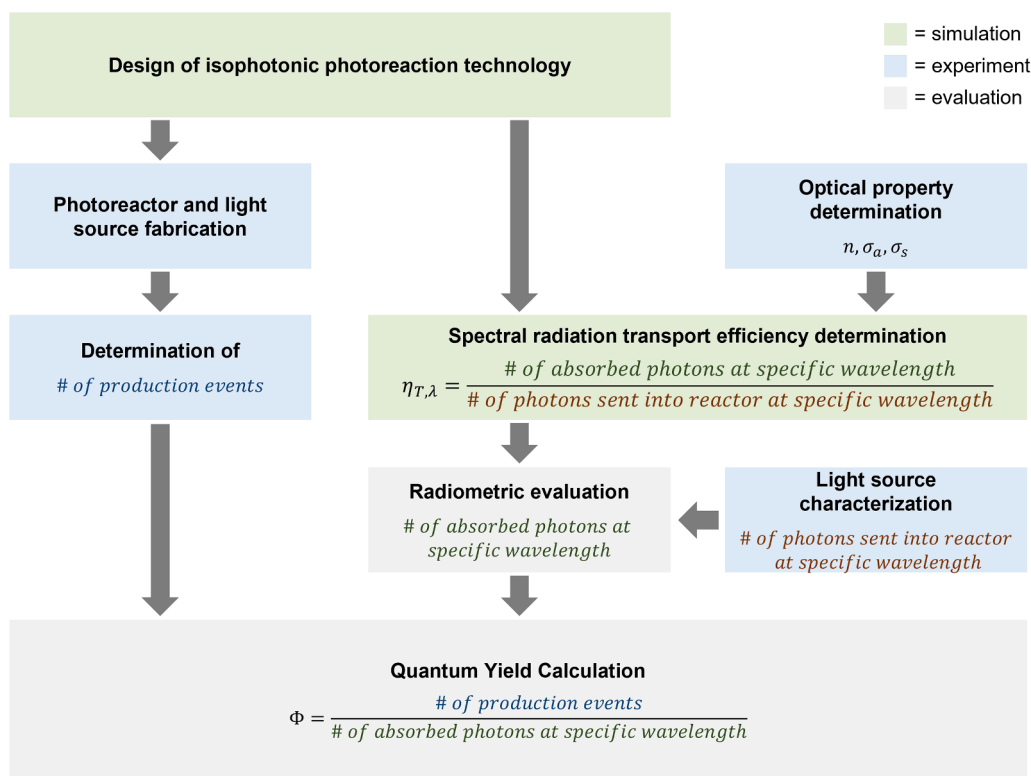
Fig. 1. Graphical summary of the proposed approach for the determination of quantum yields with isophotonic photoreaction technology. Experimental steps are highlighted in blue, simulation-based steps are highlighted in green and evaluation steps are highlighted in grey. (For interpretation of the references to colour in this figure legend, the reader is referred to the web version of this article.)
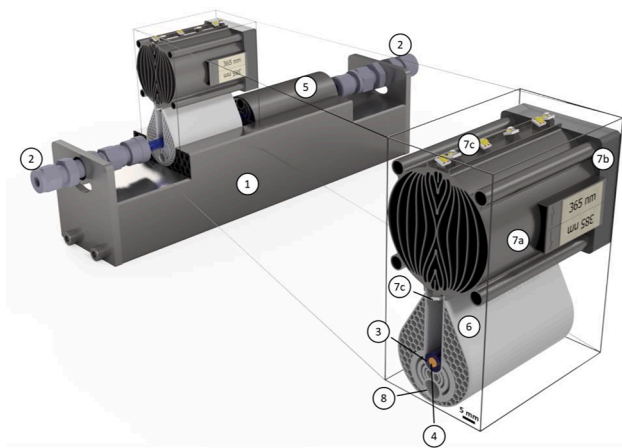
Fig. 2. CAD model of the proposed 3D-printable isophotonic photoreaction technology with zoom in on the core components. The assembly is made up of a 3D-printed body (1), fluid connectors (2), a quartz glass capillary (3) surrounding the reaction volume (4), moveable heating brackets (5), a 3D-printed and silver-coated diffuse reflecting optics module (6) and an LED light source module, made up of a 3D-printed cooler body (7a), a cooler fan (7b) and two times six high power LEDs (7c) with two different peak wavelengths, in the presentation 365 nm, facing up (being idle) and 385 nm, facing down into the reaction chamber. The temperature in the reaction zone is controlled with a heating cartridge in the optics' module heating cartridge bore (8). The black scale bar in the zoom in corresponds to 5 mm.

flow chart. The simulations are conducted considering the precise three-dimensional geometry of a tailored isophotonic photoreactor, Fig. 2, and the specific optical properties of the reactor components as well as the photocatalyst to be characterized. For details on the simulation case setup, see Appendix A. The optical properties assumed for the reactor

components and the employed photo catalysts are determined prior to any system simulation in a set of optical experiments. For details on the experimental proceeding, evaluation and resulting optical properties, see Appendix B. The simulations deliver the spectral radiation transport efficiency ($\eta_{T,\lambda}$) being defined as the ratio between the number of photons at a specific wavelength absorbed in the reaction volume by the photocatalyst considered and the number of photons sent into the reactor by the employed light source at the same specific wavelength, Eq. (3).

$$\eta_{T,\lambda} = \frac{\#of\ absorbed\ photons\ at\ specific\ wavelength}{\#of\ photons\ sent\ into\ the\ reactor\ at\ specific\ wavelength} \quad (3)$$

Consequently, to derive the number of photons absorbed by the photocatalyst placed in the reaction volume at a specific wavelength via the spectral radiation transport efficiency derived from simulations, the number of photons sent into the reactor by the employed light source must be derived experimentally via radiometric characterization of the latter.

All steps for the determination of quantum yields with the proposed approach are graphically summarized in Fig. 1.

The unique isophotonic photoreactor employed in the approach is optimized to provide a low gradient field of the local volumetric rate of photon absorption in the reaction volume. The main components of the employed photoreactor are a quartz glass tube that encloses the reaction zone, a 3D-printed, diffuse reflecting optics module placed around the quartz glass tube which disperses light into the reaction volume and lastly an LED light source module that precisely shines its light into the optics module, Fig. 2.

2. Methods

2.1. Design and fabrication of isophotonic photoreactor

The focus in the reactor design process lies on the LED light source modules, more precisely the axial position and orientation of the six symmetrically aligned LEDs. Firstly, the LEDs are alternatingly inclined for $20°$ to prevent direct illumination of the reaction zone which would lead to hotspots in the field of the local volumetric rate of photon absorption. Secondly, the axial positions of the LEDs are numerically optimized in a way that the axial course of the mean value of the local volumetric rate of photon absorption shows the lowest possible axial gradients. This simulation-based optimization task is accomplished with surrogate-based standard optimization tool surrogateopt from the MATLAB® global optimization toolbox. For the calculation of the objective function in the optimization, the reaction volume is divided in twenty equally thick slices, for illustration, see Supplementary Figure S3. In each of the slices, the mean value for the local volumetric rate of photon absorption is calculated. The objective function value subject to minimization finally equals the variance of the twenty calculated mean values.
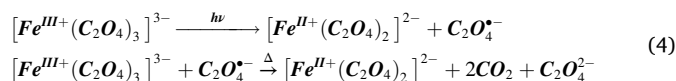
The LED position optimization depends on optical properties of the employed components. Of special interest is the dependency of the optimal LED alignment on the optical properties of the reaction volume/ the employed photo catalyst respectively. Only if the optimal positions of the LEDs on the LED light source module do not significantly depend on the optical properties of the reaction volume, a general design can be derived that is applicable to various photocatalysts. To check for a possible influence of the optical properties of the reaction volume on the optimal LED alignment, the optimization is conducted with optical properties of the reactor components at 405 nm and for different optical property sets of the reaction volume.

The derived optimal LED positions are realized practically by designing small, inclined pillars in the positions derived by the optimization onto a cooler structure equipped with a cooler fan, see zoom-in in Fig. 2. In this work, all reactor and light source structure components, namely the reactor body as depicted in Fig. 2, the optics module and the LED cooler body were printed in 316L stainless steel using a Realizer SLM 125 3D printer. The homogeneous and fine roughness of the 3D printed stainless steel substrate ensures Lambertian reflection characteristics as desired. To increase the reflectivity of the optics module after the printing process, the raw stainless steel part needs to be optically coated. In the present work, the optics module was galvanically silver coated by C. Jentner GmbH.

Lastly the LEDs of the LED light source modules must be electrically connected and mounted onto the pillar structures on the cooler body. The employed high-power LEDs with peak wavelengths of 365 nm, 385 nm, 395 nm, 405 nm, and 450 nm from by WÜRTH Electronics SE employed in this work were soldered to wires and subsequently glued onto the pillar structures on the printed LED cooler body with thermally conductive glue HERNON 746 from ALUTRONIC Kühlkörper GmbH & Co. KG.

2.2. Approach validation – Potassium ferrioxalate actinometry

Potassium ferrioxalate $(K_3[Fe(C_2O_4)_3])$ undergoes photoreduction when irradiated with photons with a wavelength smaller than 550 nm [16]. One photon thereby triggers two reduction events, Eq. (4). Since the first publications from Hatchard and Parker in 1956 reporting detailed information on the quantum yield for this reaction [17], numerous literature contributions addressed the various aspects of the potassium ferrioxalate photoreduction reaction as a chemical actinometer [18–20], which makes it a well-suited reference for the validation of the introduced approach.

$$
\begin{aligned}
\left[Fe^{III+}(C_2O_4)_3\right]^{3-} &\xrightarrow{h\nu} \left[Fe^{II+}(C_2O_4)_2\right]^{2-} + C_2O_4^{\bullet-} \\
\left[Fe^{III+}(C_2O_4)_3\right]^{3-} + C_2O_4^{\bullet-} &\xrightarrow{\Delta} \left[Fe^{II+}(C_2O_4)_2\right]^{2-} + 2CO_2 + C_2O_4^{2-}
\end{aligned}
\tag{4}
$$

The experimental proceeding employed in this work for the determination of the number of production events is adapted from the work of Lehóczki et al [20]. In the experiments 2 mM potassium ferrioxalate solution (potassium ferrioxalate, Alfa Aesar, in 0.05 M sulfuric acid, Fisher Scientific) was pumped through the photoreactor using a HITEC ZANG SyrDos™ tandem syringe pump. The concentration of the reaction product Fe^{II+} was determined in an Fe^{II+} 1,10-phenanthroline assay. In this assay 8 mL of collected sample were mixed with 3 mL 1,10-phenanthroline solution (0.1 g in 100 mL of deionized water), 4 mL of sodium acetate buffer solution (1 M sodium acetate, Arcos Organics, in deionized water mixed with 0.5 M sulfuric acid, REAGECON, in a volume ratio of 100:63), and 5 mL deionized water. The absorbance of the formed Fe^{II+}-1,10-phenathroline complex at 510 nm determined with an Agilent 8453 UV–Vis spectrometer was used to derive the desired Fe^{II+} concentration. The calibration of the assay linking the measured absorbance of the 1,10-phenathroline complex and the desired Fe^{II+} concentration was conducted with Mohr's salt solutions (Arcos Organics), see Supplementary Figure S5. In addition to the standard way via the Fe^{II+} assay, the actinometer conversion was determined online with a USB4000 UV–Vis spectrometer equipped with a FIA-Z-SMA-ULM flow cell (both Ocean Optics Inc.) that is included in the piping downstream of the photoreactor. The redundant determination increases the trustworthiness and reliability of the evaluated data set. The calibration linking the absorbance of the converted potassium ferrioxalate solution at 375 nm in the online measurement with the potassium ferrioxalate conversion was executed with synthesized actinometer solutions with different conversions prepared with potassium ferrioxalate and the commercially available reaction products iron-(II)-oxalate (Alfa Aesar) and potassium oxalate (Arcos Organics), see Supplementary Figure S5.

To properly estimate the average volumetric production rate of Fe^{II+} in the photoreactor ($\dot{r}_{Fe^{II+}}$), the actinometry experiment was conducted with three different flow rates (2.0 mL/min, 2.6 mL/min and 3.7 mL/min). The three different derived Fe^{II+} concentrations at the reactor outlet were drawn over the corresponding space time. According to a simple plug flow reactor design equation, Eq. (5), and assuming the reaction rate was constant in the reaction volume, the slope of the resulting line in this plot corresponds to the volumetric production rate of Fe^{II+}. The assumption of a constant reaction rate is valid if the local volumetric rate of photon absorption and quantum yield are constant throughout the reaction volume ($\dot{r}_{Fe^{II+}} = \Phi L_{p,\lambda}^a$).

$$
dc_{Fe^{II+}} + \dot{r}_{Fe^{II+}} d\tau = 0
\tag{5}
$$

The LED emission power in the reported experiments was chosen in a way, that the mean volumetric rate of photon absorption equalled approximately 30 mEinstein m^{-3} s^{-1}. Considering the reaction volume of approx. 0.23 mL, the potassium ferrioxalate concentration of 2 mM, the lowest feed rate employed of 2 mL/min and a quantum yield close to unity, a mean local volumetric rate of photon absorption of 30 mEinstein m^{-3} s^{-1} guarantees that the maximum conversion in the experiments is smaller than 20 %. The latter avoids precipitation of reaction products and limits conversion induced variations of the optical properties over the reactor length which would not be mapped in the optical simulations.

The average quantum yield ($\overline{\Phi}$) in the narrow emission band in which the employed LED light source module emits photons is derived via Eq. (6). Thereby V corresponds to the volume of the reaction zone in the quartz glass tube, λ to the wavelength, and $q_{p,\lambda}$ to the total spectral photon flux sent into the reactor aperture by the LED light source module.
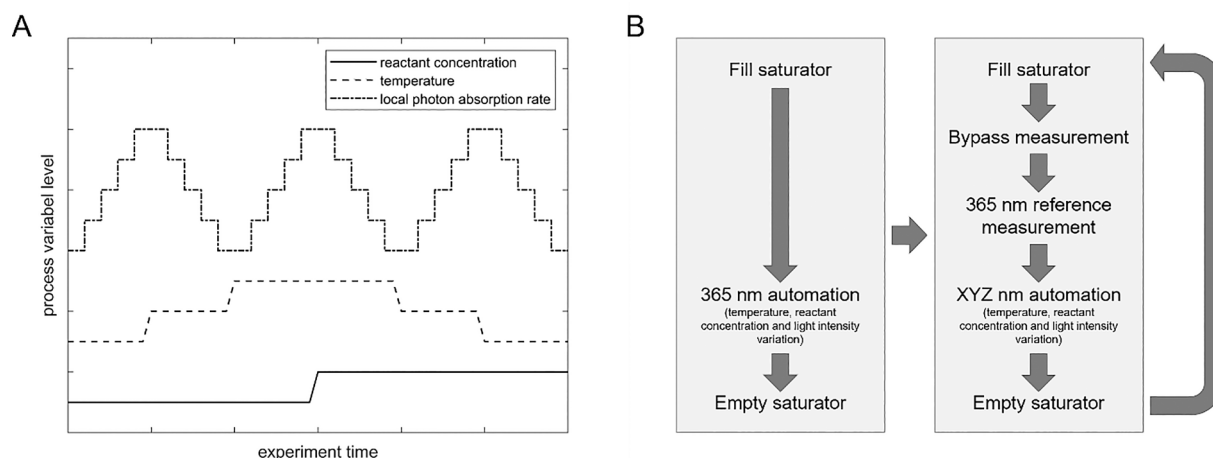
A

B

Fig. 3. A: Experiment routine executed automatically with one LED light source module in place varying reactant concentration, reactor temperature and mean local volumetric rate of photon absorption. B: Schedule of the total kinetic measurement using five different LED light source modules, including saturator refill procedures ensuring stable reactant supply and bypass and reference measurements conducted to check the catalyst for possible deactivation.

$$\overline{\Phi} = \frac{\dot{r}_{Fe^{II+}} V}{\int \eta_{T,\lambda} q_{p,\lambda} d\lambda} \qquad (6)$$

However, the quantum yield is defined at a specific wavelength, see Eq. (2), and not in an optical band. Even though the LED emission band is narrow, it is not strictly monochromatic, see Fig. C.1. Therefore, in addition to the mean values calculated by Eq. (6), estimated values of the quantum yield in narrow bands are reported. These values are derived via a least square estimation based on the assumption, that the experimentally determined mean quantum yields can be approximated via Eq. (7). Thereby $q_{p,i}$ is the photon flux in each of the narrow bands considered in the estimation, Φ_i the quantum yield in the band centre and q_p the total photon flux of the employed LED lights source module. The least square estimation minimizes the sum of residual squares between experimental mean quantum yields recorded with different LED light source modules and the quantum yields estimated by Eq. (7).

$$\overline{\Phi}_{estimated} = \sum_i \frac{q_{p,i} \Phi_i}{q_p} \qquad (7)$$

2.3. Approach application – Methanol reforming

Titania-based photocatalysts are well-known to catalyse the endothermal photo reforming reaction of alcohols [21,22], for instance methanol [23,24], at ambient conditions resulting in hydrogen as target molecule, Eq. (8). Many of the literature reported photocatalysts are straightforward to synthesize from commercial precursors and reported to be stable in operation, which makes them a suitable exemplary system for the present study.

$$CH_3OH_{(g)} + H_2O_{(g)} \xrightarrow{h\nu} CO_{2(g)} + 3H_{2(g)} \quad \Delta_R H^0 \approx 50 kJ/mol \qquad (8)$$
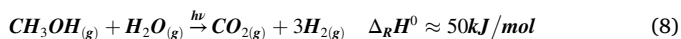
In the methanol photo reforming experiments reported, a palladium impregnated titania catalyst with 0.025 wt–% palladium loading was used. For details on the catalyst preparation see Appendix D. To ensure optical properties that allow isophotonic operation of the catalyst bed, meaning an absorption and scattering coefficient that allow penetration of photons into the reaction volume of approx. 2 mm thickness, the photocatalyst powder needs to be optically dilute. In the present work, the fine photocatalyst powder was therefore mixed with a translucent silica aerogel powder. The loading applied was 10 mg photocatalyst per mL reaction volume resulting in approximately 2.3 mg of catalyst in the reaction volume in the conducted experiments. For details on the catalyst support synthesis, powder preparation and mixing, see Appendix D.

The catalyst needs to be precisely placed in the foreseen reaction volume. The aerogel supported catalyst employed therefore was held in position in the quartz glass tube of the photoreactor by quartz glass wool plugs. The temperature of the catalyst bed in the isophotonic reactor is controlled with the optics module heating cartridge (see Fig. 2) and measured with a thermocouple axially inserted into the catalyst bed. The reactants – methanol vapour and steam – are supplied via a carrier gas stream. The carrier gas is dosed with mass flow controllers and passed through a saturator filled with a liquid methanol water mixture prior to entering the reactor. The saturator is equipped with a precise temperature control that allows the control of the methanol vapour and steam content of the carrier gas. The reactor effluent passes a pressure regulating valve and is subsequently fed into a gas chromatograph analysing the reaction products. The gas chromatograph was calibrated prior to the reported experiments for methanol, water, hydrogen, carbon dioxide, and methyl formate. All piping is electrically heated to prevent condensation of any species. Details on the test rig components and the piping and instrumentation diagram are part of the Supplementary information.

To check a possible influence of mass transport hinderances in the experiments, two control experiments with helium and nitrogen as carrier gas under high local volumetric rates of photon absorption were executed. The experiment idea is based on the approx. three times higher binary diffusion coefficient of methanol vapour in helium (approx. 3.7×10^{-5} m^2 s^{-1}, estimated via Chapman-Enskog-Wilke-Lee model) compared to the binary diffusion coefficient of methanol vapour in nitrogen (approx. 1.3×10^{-5} m^2 s^{-1}, estimated via Chapman-Enskog-Wilke-Lee model). If mass transport hinderances – both internal or external – considerably influence the apparent reaction rate, the higher diffusivity of methanol vapour in helium compared to nitrogen as carrier gas leads to a significant difference in the observed apparent reaction rates in the experiments with helium and nitrogen. If no such influence can be observed mass transport hinderances can be neglected in the considerations.

For each of the employed LED light source modules, the LED light source emission power was varied through a drive current variation in five levels to vary the volume average local volumetric rate of photon absorption between zero (dark reference) and approximately 100 μEinstein g$_{Cat}^{-1}$ s^{-1}. On a side note, the local volumetric rate of photon absorption can be given volume or catalyst mass specific. The two metrics are connected via the catalyst volumetric loading in the reaction volume. The reactor temperature was varied in three levels from 60 °C over 80 °C to 100 °C. The reactant concentration was varied in two levels

Table 1

Derived optimal axial LED positions resulting in a minimal axial gradient in the radial mean value of the local volumetric rate of photon absorption. Values are indicated for different absorption and scattering coefficients of the reaction volume. The employed LED numbering is graphically highlighted in Fig. 4 for clarification.

Absorption coefficient / m^{-1}	Scattering coefficient / m^{-1}	Position / mm (measured from cooler body front/back face)		
		LED I & VI	LED II & V	LED III & IV
200	0	1.70	6.48	20.06
200	450	1.70	6.51	19.47
200	900	1.70	6.47	19.78
400	0	1.70	6.48	20.48
400	450	1.70	6.49	20.23
400	900	1.70	6.52	19.79
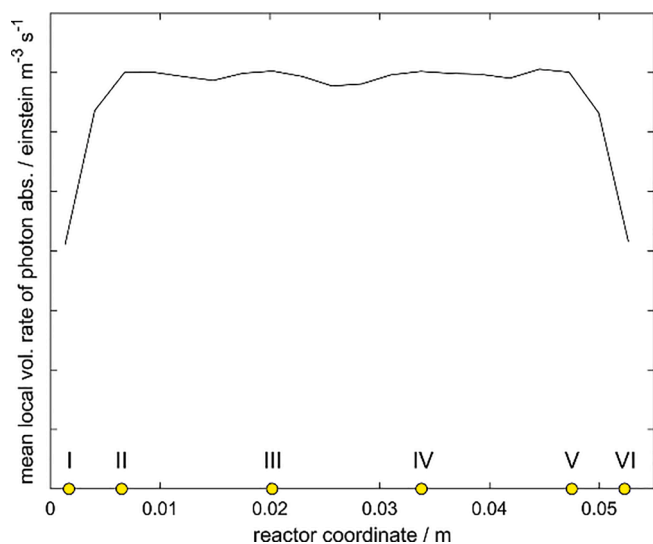
Fig. 4. Simulated axial course of the mean local volumetric rate of photon absorption in the reaction volume after optimization of the LED positions on the LED light source modules at a wavelength of 405 nm with the exemplary optical properties of the reaction volume (absorption coefficient of 200 m^{-1} and scattering coefficient of 450 m^{-1}). The yellow circles on the x-axis indicate the derived optimal axial positions of the six LEDs of the LED light source module. The Arabic numbers refer to the LED numbering in Table 1. (For interpretation of the references to colour in this figure legend, the reader is referred to the web version of this article.)

of approx. 3 mol–% and approx. 4 mol–%. The system pressure and carrier gas feed rate were kept constant at 0.5 bar relative and 5 mL$_N$ min^{-1}, respectively. The experiment design comprised a full factor variation resulting in 30 operating points per LED light source module, Fig. 3A. Each operating point was measured three times before the next operating point was set.

To ensure stable reactant feed supply, the saturator was refilled with fresh methanol water mixture before each experiment set with one of the five LED light source modules. Additionally, after each saturator refill, a bypass measurement was conducted to check the reactant feed concentration.

To verify the catalyst is not deactivated, a reference measurement with the 365 nm LED light source module, at 60 °C reactor temperature, a reactant feed concentration of approx. 3 mol-% and a volume average local volumetric rate of photon absorption of approximately 20 μEinstein g$_{Cat}^{-1}$ s^{-1} was executed before each experiment with a new LED light source module. A flow chart of the whole experimental proceeding including all LED light source module changes, saturator refill procedures as well as bypass and reference measurements is depicted in Fig. 3B.

The average quantum yield ($\overline{\Phi}_{H_2}$) in the emission band of the employed LED light source module is derived based on the number of reduced hydrogen atoms. The latter corresponds to the number of produced hydrogen molecules derived from the experimentally determined hydrogen molar fraction (y_{H_2}) multiplied by the number of two electrons per hydrogen molecule (n_{e^-,H_2}), Eq. (9). Thereby $\dot{N}_{N_2}$ corresponds to the carrier gas feed rate and y_{N_2} to the molar fraction of nitrogen in the reactor effluent.

$$\overline{\Phi}_{H_2} = \frac{\dot{N}_{N_2} \frac{y_{H_2}}{y_{N_2}} n_{e^-,H_2}}{\int \eta_{T,\lambda} q_{p,\lambda} d\lambda} \qquad (9)$$

3. Results and discussion

3.1. Radiation transport simulations

3.1.1. Optimal LED positions

The LED positions derived in the alignment optimization assuming different optical properties of the reaction volume result in the LEDs next to the front and back face of the LED light source module being slightly closer to each other compared to the LEDs in the centre, see Table 1. For an illustration of this clustering of LEDs near the front and back face of the LED light source module, see zoom in in the CAD model rendering in Fig. 2.

As evident from the optimal LED alignment parameter values listed in Table 1, the optimal LED alignment only slightly depends on the optical properties of the reaction volume. Since the deviations lie in the range of the manufacturing accuracy of the LED light source modules (roughly ± 400 μm), the LED light source modules do not need to be adjusted to a specific photocatalyst with its individual optical properties. However, a verification of the design criterion of an isophotonic reaction volume is advised for each photocatalyst considered. This especially holds since radial gradients that might occur as a consequence of a radiation transport hinderance in the photocatalyst bed are not addressed in the optimization. The verification should be based on the density distribution of the local volumetric rate of photon absorption as described in Section 3.1.2.

In the presented work, the realized optimal centre positions of the first, second, and third LED counted from the front face of the 54 mm long optics module were 1.7 mm, 6.5 mm, and 20.2 mm, respectively. For an illustration of the positioning, see yellow circles in Fig. 4. With the clustering of LEDs near the front and back face, the optimization algorithm compensates photon losses over the front and back face opening of the optics module resulting in an almost constant axial course of the mean local volumetric rate of photon absorption throughout the reaction volume, Fig. 4. On a side note, non-ideal LED alignments significantly deteriorate the homogeneity of the local volumetric rate of photon absorption, see axial absorption profiles resulting under non-ideal LED alignments in Supplementary Figure S4.

3.1.2. Photocatalyst simulations

The simulations mapping the radiation transport problem in both, the validation experiment – the potassium ferrioxalate actinometry – and the exemplary use case – the photo methanol reforming experiment – assumed the accordingly derived optimal LED alignment. The simulations give access to the spectral radiation transport efficiency needed for the quantum yield calculations following Eqs. (6) and (9), Fig. 5. Additionally, they reveal the density distributions of the local volumetric rate of photon absorption needed for the assessment of the homogeneity of the field of the local volumetric rate of photon absorption, insets Fig. 5.

The similar characteristic course of the spectral radiation transport efficiency in the two simulation sets presented in Fig. 5 with a significantly higher spectral radiation transport efficiency in the UV band compared to the Vis band is induced by a significantly higher absorption
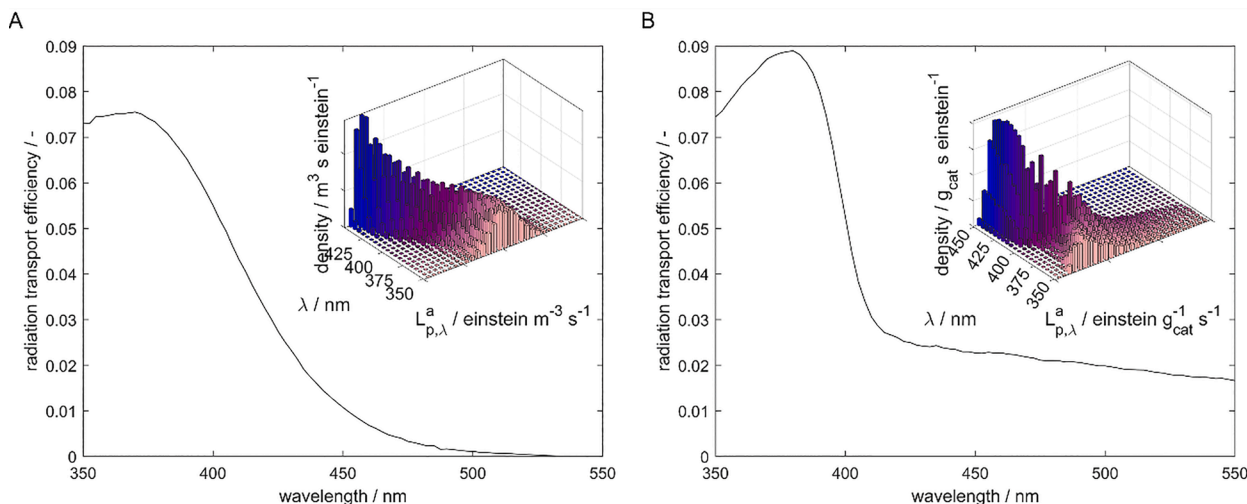
Fig. 5. Simulated spectral radiation transport efficiencies in the optical band from 350 nm to 550 nm (primary graphs) and density distributions of the local spectral volumetric rate of photon absorption in the optical band from 350 nm to 450 nm (insets) for both, the potassium ferrioxalate actinometry experiments (A) and the methanol reforming experiment (B). The spectral resolution in the simulations was 2.5 nm.
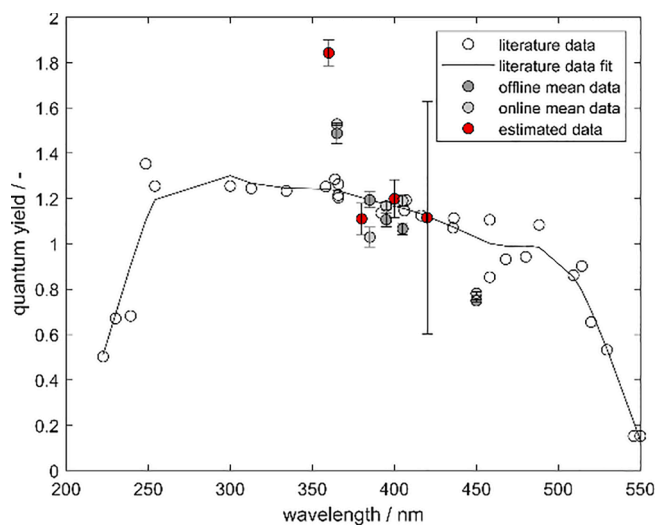
Fig. 6. Mean quantum yields determined via Fe^{II+}-assay and online UV–Vis spectroscopy at a mean local volumetric rate of photon absorption of approximately 30 mEinstein m^{-3} s^{-1} (solid circles, dark and light grey) together with estimated quantum yields in 20 nm wide bands between 350 nm and 410 nm (solid circles, red) in comparison with literature data [25] (open circles). Indicated error bars of experimental data are errors propagated from the determination of the Fe^{II+} reaction rate and thereby represent the experimental error. Indicated error bars of the estimated data correspond to one standard error derived in the quantum yield estimation in narrow bands. (For interpretation of the references to colour in this figure legend, the reader is referred to the web version of this article.)

coefficients in the UV band compared to the Vis band in both material systems, compare Fig. B.2. The obvious differences between the optical properties of the two systems, especially regarding the absolute values of the absorption and scattering coefficient, however, lead to significantly different density distributions of the local volumetric rate of photon absorption, see insets Fig. 5. Whereas the design goal of an isophotonic reaction volume is precisely fulfilled for the potassium ferrioxalate system, the methanol reforming system shows a slightly broadened density distribution of the local volumetric rate of photon absorption especially for wavelengths below approx. 375 nm.
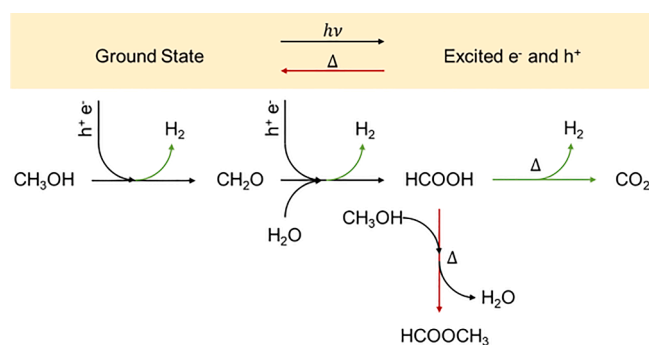
Fig. 7. Proposed reaction network in the methanol reforming system mapping oxidation of methanol (CH_3OH) to carbon dioxide (CO_2) with the two intermediates formaldehyde (CH_2O) and formic acid ($HCOOH$) and methyl formate as side product. The yellow box depicts the photon induced charge carrier dynamics that precedes the depicted chemical reactions including both charge carrier generation via photon absorption and charge carrier recombination in non-radiative processes. The reaction arrows highlighted in green and red indicate thermally activated processes that increase (green) or decrease (red) the quantum yield with increasing temperature, respectively. (For interpretation of the references to colour in this figure legend, the reader is referred to the web version of this article.)

3.2. Method validation – Potassium ferrioxalate actinometry

The mean quantum yields derived via Eq. (6) for the potassium ferrioxalate system are already in good agreement with literature data [25] and thereby indicate the validity of the proposed approach, dark and light grey circles in Fig. 6. Additionally, the estimated quantum yields in four 20 nm wide bands between 350 nm and 410 nm support the interim conclusion of a valid approach, red circles in Fig. 6. The applicability of the proposed approach for the determination of quantum yields under isophotonic conditions is thereby successfully validated and the scheme presented in Fig. 1 can be applied to any photocatalyst. Noteworthy, the outlier at the lower end of the experimentally covered optical band in Fig. 6 can be attributed to the unfortunate device-specific inaccuracy of the determination of the LED light source module emission at wavelengths below 370 nm, discussion see Appendix C. The high standard deviations in the band from 390 nm to 410 nm results from lower emission power of the employed LED light source modules in this band and a thereby induced lower sensitivity of the estimation model towards
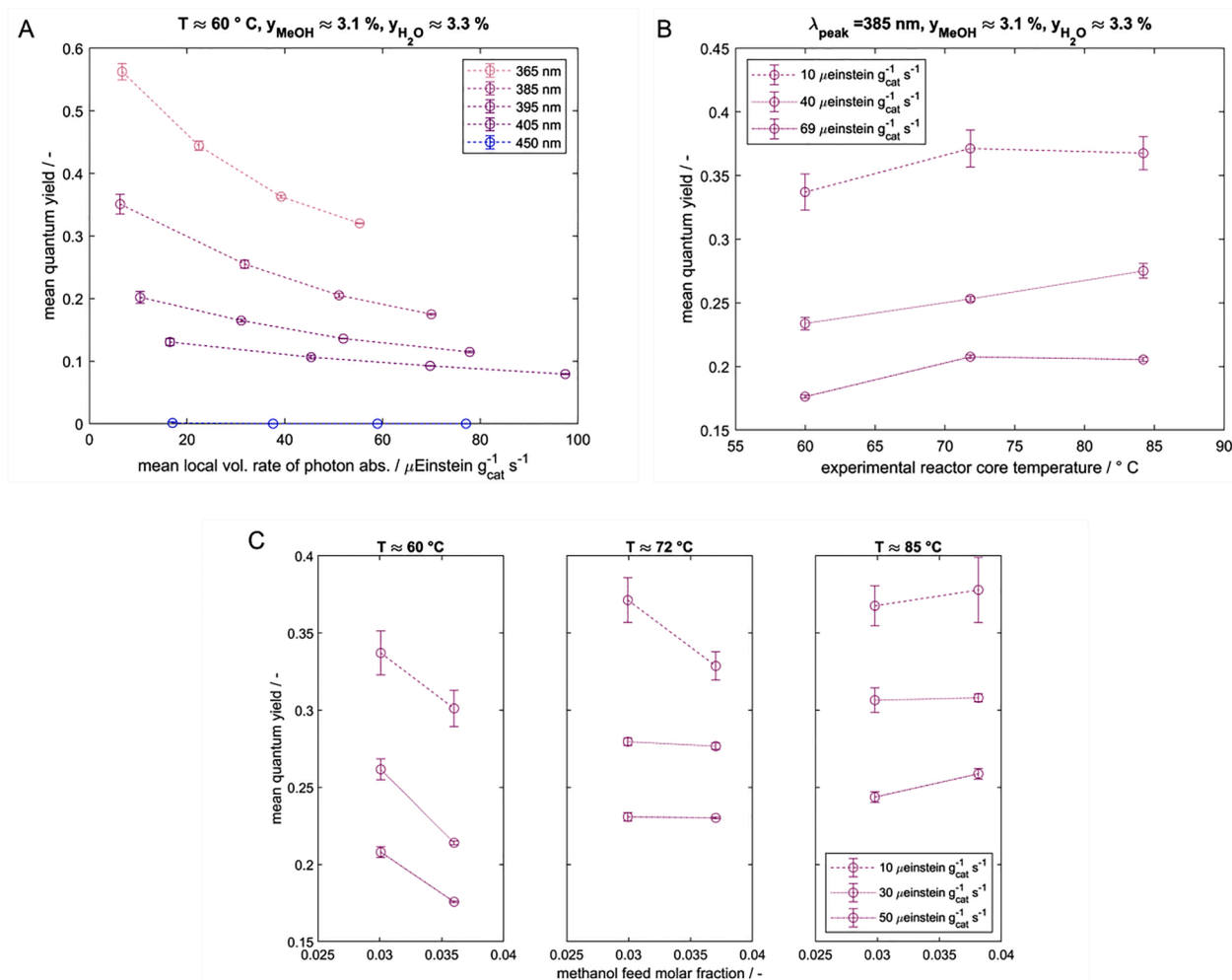
Fig. 8. Determined mean quantum yields in the methanol photo reforming experiments. A: Dependency of the mean quantum yield on the mean local volumetric rate of photon absorption at different LED light source module peak wavelengths between 365 nm and 450 nm, a reactor temperature of 60 °C and methanol and steam feed concentrations of 3.1 % and 3.3 % respectively. B: Dependency of the mean quantum yield on the reactor core temperature at three different mean photon absorption rates between 10 and 69 μEinstein g_{cat}^{-1} s^{-1}, a wavelength of 385 nm and methanol and steam feed concentrations of 3.1 % and 3.3 %. C: Dependency of the mean quantum yield on the methanol feed concentration for different mean local volumetric rates of photon absorption between 10 and 50 μEinstein g_{cat}^{-1} s^{-1} at three different reactor temperatures between 60 °C and 85 °C and a fixed peak wavelength of 385 nm. Error bars are derived via error propagation of the standard deviations of the measured species concentrations based on three repetition measurements.

the quantum yield in this band. Higher wavelength specific resolution, or narrower bands for the quantum yield estimation respectively, would only be possible with more employed light source modules with peak wavelengths differing from those already employed.

3.3. Exemplary application – Methanol photoreforming

The methanol photo reforming experiments conducted with the exemplary titania-based catalyst revealed significant hydrogen production rates up to 32 mmol H_2 g_{cat}^{-1} h^{-1} and a neglectable dark activity below the detection limit of the employed gas chromatograph (which equals approx. 0.2 mmol H_2 g_{cat}^{-1} h^{-1}). The carbonaceous reaction products detected in the experiments were carbon dioxide and methyl formate with traces of formaldehyde at certain operating points supporting the proposed reaction network depicted in Fig. 7. Importantly the catalyst did not show significant deactivation in the more than 500 h on stream with constantly changing operating conditions, see reference measurements Supplementary Figure S8. Furthermore, the data from the experiment conducted to check for a possible influence of mass transport hindrances in the kinetic measurements indicates these can be neglected in the considerations, see Supplementary Figure S7. On a side note, the

photocatalyst bed temperature, detected with a thermocouple placed at the reactor inlet, was increased through the absorption of photons by maximum 1.5 K in the experiments.

The mean quantum yields derived via Eq. (9) for the methanol reforming system are with maximum values of almost 60 % astonishingly high for a simple, only slightly modified commercial catalyst system and obviously depend on all varied process conditions, Fig. 8. The nature of these dependencies is complex. The clearest influence however shows the conducted wavelength variation. Whereas the mean quantum yield recorded using the 365 nm LED light source module lies between 60 % and 30 %, the experiment with the 450 nm LED light source module did not depict any significant hydrogen production rate and thus resulted in quantum yields close to zero, Fig. 8A. This observation is to be expected since the estimated band gap of the employed titania-based catalyst system lies just above 400 nm. For details on the band gap estimation, see Appendix B. Photons from the 450 nm LED light source module, all having a wavelength larger than 400 nm, therefore, cannot excite electrons into the conduction band and consequently cannot induce any photoreaction. This finally leads to an apparently 'dead' catalyst in the experiments with the 450 nm LED light source module. The position of the band gap might also explain some of the UV-band
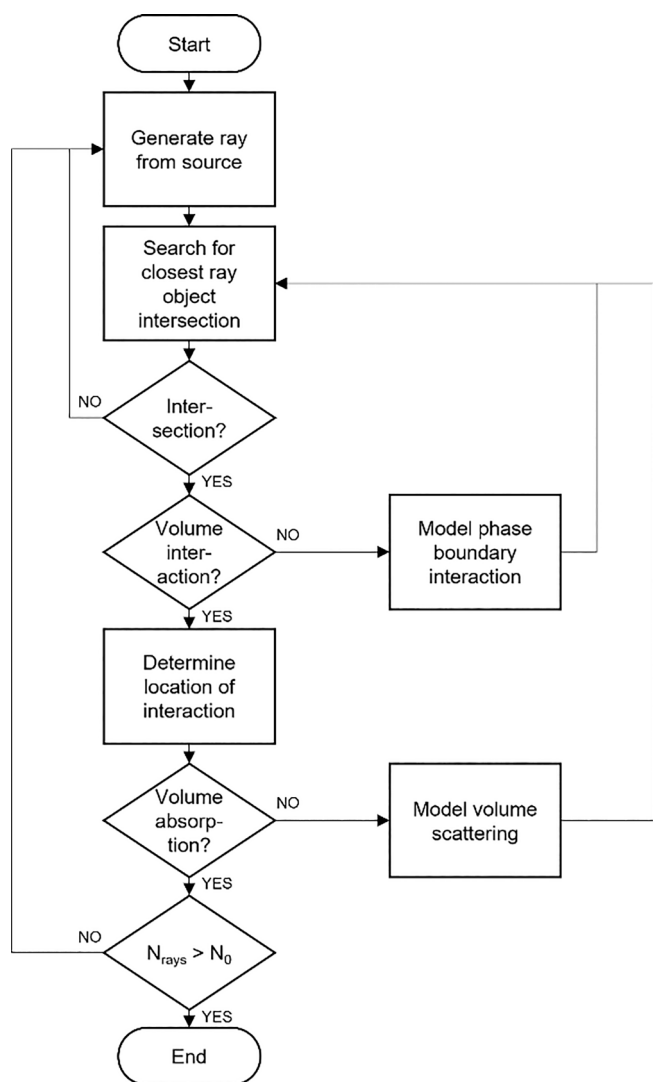
Fig. A.1. Code flow chart of the implemented Monte Carlo ray tracing method highlighting the repeatedly executed steps of ray generation, intersection search and interaction modelling on phase boundaries and in volumes. The flow chart is drawn in accordance with DIN66001.

internal variation of the mean quantum yield evident in Fig. 8A. With increasing peak wavelength of the LED light source modules, the determined mean quantum yield observably decreases. This effect is partially a consequence of the band gap position since with increasing peak wavelength of the LED light source modules, more and more photons from the not ideally monochromatic LEDs have a wavelength above the band gap wavelength of 400 nm, see Fig. C.1A. These photons with insufficient energy to surpass the band gap do not induce any photoreaction but nevertheless contribute to the calculated mean local volumetric rate of photon absorption which results in smaller calculated mean quantum yields. Noteworthy, the position of the band gap cannot fully explain the observed spectral dependency of the quantum yield. The quantum yields determined with the LED light source modules with emission peak wavelengths of 385 nm and 395 nm for instance, lie, depending on the mean local volumetric rate of photon absorption, between 45 % and 35 % (relative) apart. At the same time, the share of photons with an energy above the band gap energy emitted by the two LED light source modules lie only roughly 25 % (relative) apart.

Besides the wavelength dependency of the experimentally determined mean quantum yields, the influence of the mean local volumetric rate of photon absorption has the second strongest experimentally observed influence on the performance of the employed catalyst system, see Fig. 8A. Increasing the mean local volumetric rate of photon absorption reduces the observed mean quantum yield throughout all operating points with different LED light source modules, under all reaction temperatures and reactant feed concentrations examined in this work. This effect could be the consequence of an intensification of non-radiative relaxation processes of photon-induced charge carriers with increasing charge carrier generation density under intensified local photon absorption, red reaction arrow in yellow box Fig. 7.

The observed dependency of the determined mean quantum yields on temperature is less straight forward and less significant than the wavelength and local volumetric rate of photon absorption dependencies. The exemplary data set presented in Fig. 8B shows the mean quantum yield drawn over the catalyst bed temperature at different mean local volumetric rates of photon absorption and an LED light source module peak wavelength of 385 nm. At the depicted low and high mean local volumetric rates of photon absorption of 10 and 69 µEinstein g_{cat}^{-1} s^{-1}, the temperature courses indicate an optimum temperature between 70 °C and 80 °C at which the mean quantum yield peaks. In contrast to that, the temperature course of the mean quantum yield at an intermediate local volumetric rate of photon absorption of 40 µEinstein g_{cat}^{-1} s^{-1} depicts a continuous increase of the mean quantum yield with increasing temperature. This complex behaviour of the examined photocatalyst can be interpreted as an indication for multiple competing thermally activated processes in the underlying reaction network, coloured reaction arrows in Fig. 7. An increase of the mean quantum yield with increasing temperature can be explained with an intensification of thermally driven desorption processes of the reaction products and, of higher importance, with an intensification of thermally driven decomposition of the reaction intermediate formic acid on the palladium co-catalyst to carbon dioxide and hydrogen, green highlighted reaction arrows in Fig. 7. A decrease of the mean quantum yield with increasing temperature could be explained by a thermal intensification of non-radiative charge carrier recombination processes leading to less excited charge carriers that can drive chemical reactions. Additionally, the competitive thermal reaction of the reaction intermediate formic acid and the methanol feed to methyl formate reduces the mean quantum yield, red highlighted arrows in Fig. 7. Both, the decomposition reaction of formic acid and the side reaction of formic acid with methanol, are likely to be influenced by the process intensity or the local volumetric rate of photon absorption, because the concentration of the reaction intermediate formic acid is likely to be higher if the photoreaction of methanol to formaldehyde and further to formic acid is enhanced. In the exemplary data depicted in Fig. 8B, the appearance of a temperature optimum between 70 and 80 °C at low mean local volumetric rate of photon absorption could result from an intensification of the thermal side reaction of formic acid to methanol with increasing temperature. Increasing the mean local volumetric rate of photon absorption from 10 µEinstein g_{cat}^{-1} s^{-1} to 40 µEinstein g_{cat}^{-1} s^{-1} apparently favours the decomposition reaction of formic acid rather than the side reaction towards methyl formate leading to the observed monotonous increase of the mean quantum yield with increasing temperature at intermediate local volumetric rate of photon absorption. This is an indication for different substrate concentration sensitivities of the two reactions that formic acid undergoes with the decomposition reaction being slightly more sensitive towards the formic acid concentration. The appearance of a temperature optimum at high mean local volumetric rate of photon absorption of 69 µEinstein g_{cat}^{-1} s^{-1} depicted in Fig. 8B could be shaped by the temperature dependency of non-radiative charge carrier recombination processes being more relevant at higher charge carrier generation densities or local volumetric rates of photon absorption respectively.

The influence of the methanol feed concentration on the mean quantum yield depicted in Fig. 8C, is a further indication of the influence of the two reactions of formic acid onto the mean quantum yield. At lower reactor temperatures and especially for lower mean local
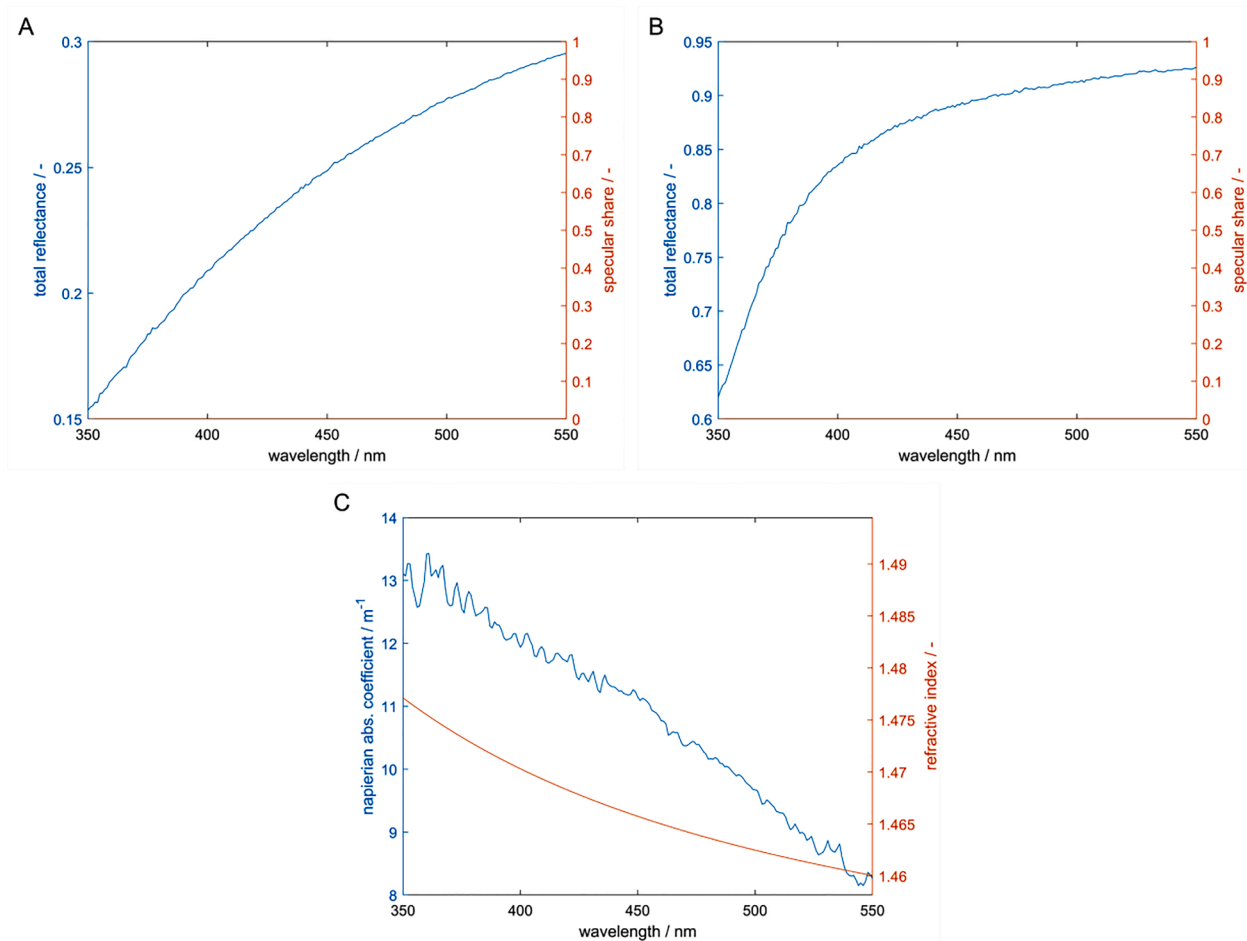
Fig. B.1. Optical properties measured and assumed for the simulations for all reactor components. A: printed 316L cooler of the LED modules, B: cavity silver coating, C: quartz glass tubing.
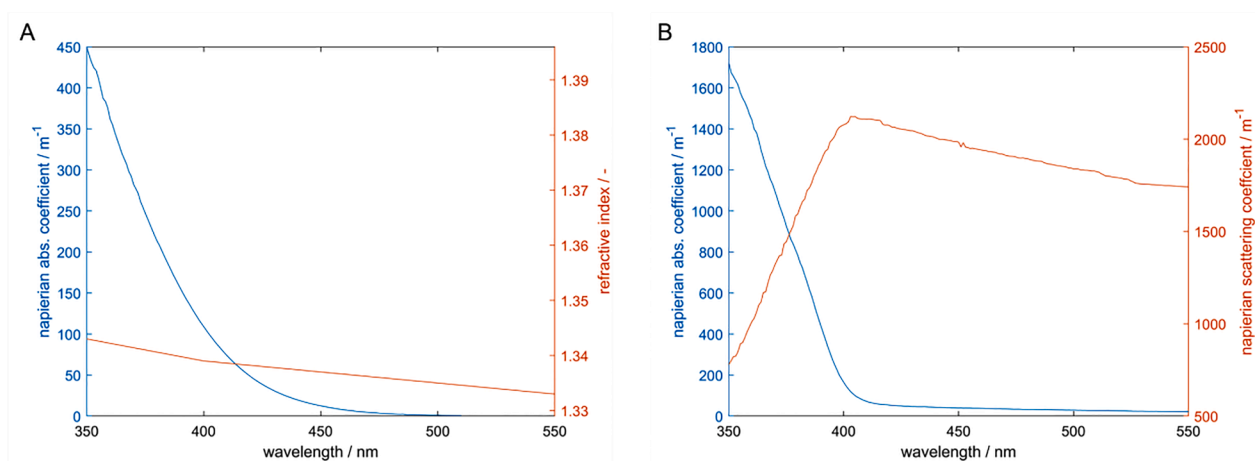

Fig. B.2. Optical properties of the 2 mM ferrioxalate solution employed in the actinometry experiments (A) and catalyst bed employed in the methanol reforming experiments (B).

volumetric rates of photon absorption, higher methanol feed concentrations induce a slight drop of the determined mean quantum yield indicating that the side reaction towards methyl formate dominates the concentration dependency of the mean quantum yield. The picture inverts for high mean local volumetric rates of photon absorption and increased temperature, where increasing the methanol feed concentration results in a slight increase of the mean quantum yields indicating

that the photoreaction towards formic acid and its subsequent decomposition determines the concentration dependency of the mean quantum yield.

Summarizing, the titania-based photo reforming system is complex in its nature due to multiple competing processes being influenced by all varied operation conditions, namely temperature, reactant concentration, wavelength, and local volumetric rate of photon absorption.
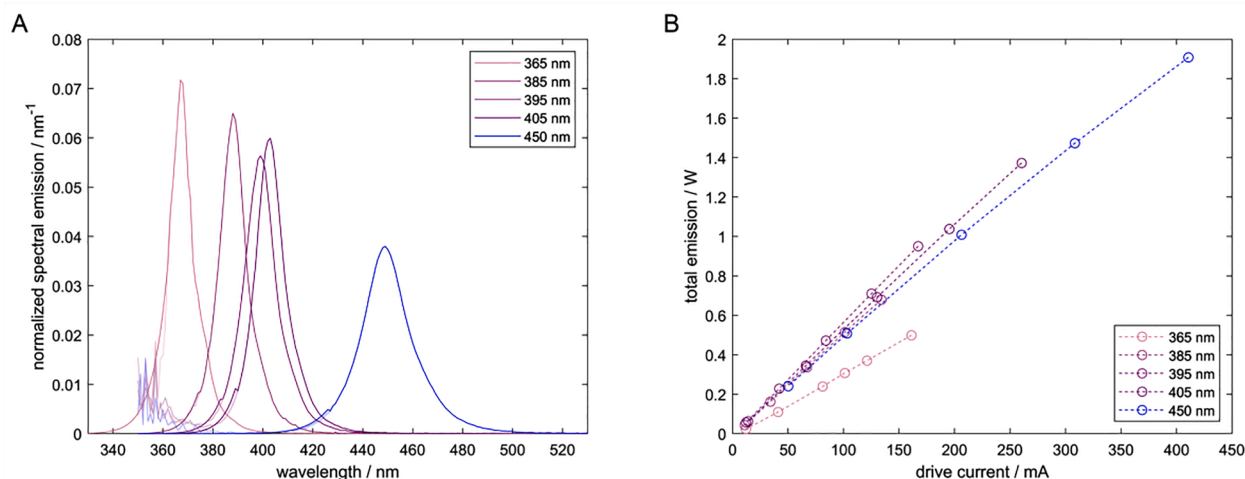
Fig. C.1. Measured emission spectra for all five employed LED light source modules normalized to have an area equal to unity (A). Current total emission characteristics measured for all LED light source modules (B).

Noteworthy the 'photon-related' operation conditions, wavelength, and local volumetric rate of photon absorption, show the strongest influence on the quantum yield. In the varied ranges, temperature and reactant concentration play a minor role.

4. Conclusion and perspective

The introduced approach for the determination of quantum yields in gas, liquid, and multi-phase photoreactions could successfully be validated via the determination of the quantum yield of the well-known potassium ferrioxalate actinometer. Further the approach's adaptability could be demonstrated with an application to an exemplary aerogel-supported titania-based methanol photo reforming catalyst system. The novel isophotonic photo reactor employed allowed to precisely vary wavelength, local volumetric rate of photon absorption, temperature, and reactants' concentration in the conducted photo reforming experiments.

Thereby, from the chemical engineering point of view, the observation of a decreasing quantum yield with increasing local volumetric rate of photon absorption is of utmost importance. The local volumetric rate of photon absorption translates to the process intensity and thereby dictates the size of the reactor and the amount of catalyst needed to achieve a desired production in a production photoreactor. With the quantum yield of a photocatalytic system decreasing with increasing local volumetric rate of photon absorption, challenging optimisation issues arise. They demand a trade-off between high achieved photocatalytic efficiency and low capital invest for smaller apparatuses comprising less catalyst. Additionally, in a slightly broader view, the finding of decreasing quantum yields with increasing local volumetric rate of photon absorption also indicates that the design of high efficiency production photoreactors not only demands for efficient photon transport from the light source or reactor aperture into the reaction volume, but also an adequate photon distribution in the reaction volume to avoid hot spots in the field of the local volumetric rate of photon absorption to a reasonable extend.

Further, from a material science point of view, the dependency of the quantum yield on the local volumetric rate of photon absorption is of outstanding importance. When reporting quantum yields or comparing different photocatalysts with each other the local volumetric rate of photon absorption should be indicated according to the findings depicted above. This claim is in line with recent reports on the quantum yield of the potassium ferrioxalate system indicating that the quantum yield drops under very intense photon absorption [19]. It is also in good agreement with reports of observed photocatalytic efficiencies in

photocatalytic processes being dependent on the intensity of the employed light source [23]. In best case, quantum yields would be determined using photoreactors providing isophotonic reaction conditions in analogy to the requirement that thermal reaction kinetics should be determined in isothermal reactors.

Further development of the proposed approach should address the LED light source modules that currently show narrow but not monochromatic emission spectra. To achieve higher wavelength resolution and access quantum yield data directly without the detour over mean quantum yields with subsequent quantum yield estimations, as showcased with the data from the potassium ferrioxalate system, filters should be used to reduce the band width of the photons sent into the reactor.

For a maximum reliability of the necessary optical simulations, detailed knowledge of the radiation transport properties is essential. In the present work, radiation transport properties were experimentally determined prior to any simulation. Thereby, the assumption of isotropic scattering characteristics of the photocatalyst bed is a simplification. Particles typically depict complex scattering characteristics depending on the particle shape and material. In future work, this issue should be addressed in more detailed optical characterisations of the photocatalysts employed.

To facilitate the adaptation and development of the approach by researchers in the field, all STEP files needed for 3D-printing of the reactor components as well as a MATLAB® toolbox needed for the optical simulations are published alongside this publication via KITO-penData [31] . The published MATLAB® toolbox comprises the employed MCRT simulation environment with an easy-to-use function to derive all needed simulation data for quantum yield estimations according to the proposed approach. It can also be used to setup and run user-defined optical simulations.

Declaration of Competing Interest

The authors declare that they have no known competing financial interests or personal relationships that could have appeared to influence the work reported in this paper.

Data availability

CAD print files for the reported 3D-printable photoreactor and a MATLAB® toolbox with tools for Monte Carlo ray tracing and reproduction of the reported simulations are provided alongside the publication. Further data will be made available on request.

Appendix A. . Radiation transport modelling

The optical simulations in this work are conducted with an in-house developed MATLAB®-based implementation of an Monte Carlo ray tracing method. Briefly 'a large number' of rays carrying each a share of the total light source emission are generated on the light sources' surfaces and sent into the simulation domain including all objects (=components) to be mapped. The rays are then traced on their way through the domain interacting with the objects until they are either absorbed by an object or miss any of the objects comprised in the simulation domain. The photons carried by an absorbed ray are accounted to the object that absorbed it, more specifically to the surface or volume element in which they are absorbed. The superposition of many absorption events or simulated rays respectively approximates the solution of the radiation transport problem. To give a better idea of the implementation and the method, a code flow chart summarizing the Monte Carlo ray tracing procedure is given in Fig. A.1.

The physics mapped on the rays' paths include absorption and scattering in volumes, refraction, partial reflection on phase boundaries and absorption and reflection on non-transparent surfaces. Mathematically, the attenuation of a ray's intensity (I) traveling in direction of the ray direction normal vector (n) in an absorbing and/or scattering medium with an absorption and a scattering coefficient (σ_a and σ_s) is modelled according to Lambert-Beer's law, Eq. (A.1). In the presented work, scattering is assumed to be isotropic and leads to an alteration of the ray direction in the scattering centre. On a side note, other than isotropic scattering characteristics, if known, can be mapped as well.

$$n \bullet \nabla \boldsymbol{I} = -(\boldsymbol{\sigma_a} + \boldsymbol{\sigma_s})\boldsymbol{I} \tag{A.1}$$

Refraction and partial reflection with a given reflectivity (R) on phase boundaries are modelled according to Snell's law and the Fresnel equations, Eqs. (A.2) and (A.3). n_1 and n_2 are the refractive indices of the media in contact at the phase boundary and α and β the incidence angle and angle of refraction respectively.

$$\frac{\boldsymbol{\sin\beta}}{\boldsymbol{\sin\alpha}} = \frac{\boldsymbol{n_1}}{\boldsymbol{n_2}} \tag{A.2}$$

$$R = \begin{cases} \dfrac{1}{2}\left[\dfrac{\sin^2(\alpha-\beta)}{\sin^2(\alpha+\beta)} + \dfrac{\tan^2(\alpha-\beta)}{\tan^2(\alpha+\beta)}\right], \ \alpha \neq 0° \\[4mm] \left(\dfrac{n_1-n_0}{n_1+n_0}\right)^2, \ \alpha = 0° \end{cases} \tag{A.3}$$

Reflection on the surface of non-transparent surfaces is modelled via a simple reflection law, Eq. (A.4), mapping the ray's intensity after a reflection being equal to the incident ray intensity (I_0) multiplied with the reflectivity (R). The reflection is thereby assumed to be specular, ideally diffuse (Lambertian) or a combination of both with a defined specular share.

$$\boldsymbol{I} = \boldsymbol{R}\boldsymbol{I_0} \tag{A.4}$$

The simulation environment was validated against standard literature models including partial reflection and refraction on windows, attenuation in an absorbing volume and diffuse reflection of optically thick layers, details see Supplementary Figure S2 or corresponding folder of the MATLAB® toolbox provided alongside this contribution.

In the reported simulations the simulation domain comprised the LED cooler body, the optics module, the quartz glass capillary, and the reaction volume, zoom in in Fig. 2. The LED cooler body and the optics module were modelled as non-transparent ideally diffuse reflecting objects with wavelength dependent reflectivity. The quartz glass tubing was modelled as a transparent object with a wavelength-dependent refractive index and absorption coefficient. For the validation experiment – the determination of the quantum yield of the potassium ferrioxalate actinometer – the reaction volume was modelled as a transparent object with wavelength dependent refractive index and absorption coefficient. For the determination of the quantum yield of the titania-based methanol reforming catalyst, a scattering coefficient of the reaction volume was considered in addition. All optical properties were determined experimentally prior to the simulations or taken from literature references, details see Appendix B.

The light sources in the simulations were six Lambertian emitters with rectangular surfaces corresponding to the six LEDs of the LED light source modules. The Lambertian characteristics and geometric dimensions of the emitting surfaces were taken from the technical data sheet of the employed LEDs. The spectral photon flux emitted by the five employed LED light source modules ($q_{p,\lambda}$) was determined experimentally prior to simulations via detailed radiometric measurements, details see Appendix C.

The target metric of the simulations reported, the spectral radiation transport efficiency as defined in Eq. (3), is derived from ray counts relating the number of rays absorbed by the reaction volume to the number of rays emitted by the six mapped LED light sources, Eq. (A.5).

$$\eta_{T,\lambda} = \frac{\#\textit{of rays absorbed by the reaction volume}}{\#\textit{of rays emitted by the LED light source module}} \tag{A.5}$$

The second target metric reported, the density distribution of the local volumetric rate of photon absorption, is derived from absorbed ray counts in voxels that together shape the cylindrical reaction volume in the quartz glass tube. The local volumetric rate of photon absorption in one voxel is thereby calculated via relating the number of absorbed rays in the voxel to the number of simulated rays and the voxels' volume. Weighting with the spectral emission of the LED light source modules finally delivers the local volumetric rate of photon absorption.

The number of rays needed to achieve convergence in the spectral radiation transport efficiency is chosen in a way that the relative standard deviation in five repeat simulations is well below one percent in an exemplary case. This number equalled two million rays per case. The computation time per case under these conditions on a workstation equipped with an AMD Ryzen Threadripper^{TM} 3960X CPU is between 60 s and 120 s per simulation case.

Appendix B. . Optical property determination

The reflectivity of the LED cooler body's 316 L surface and the optics module's silver coating, Fig. B.1A and B, were derived from diffuse reflectance measurements using a Perkin Elmer Lambda 1050 UV–Vis spectrometer equipped with an integrating sphere assembly. For accurate measurements, the data was recorded relative to a Zenith Polymer diffuse reflection standard from Sphere Optics GmbH and corrected accordingly.

The Napierian absorption coefficient and refractive index of the employed Ilmasil PN quartz glass reaction tube purchased from QSIL GmbH, Fig. B.1C, were derived from manufacturer indications on the transmittance of quartz glass samples with thicknesses of 1.0 mm, 1.5 mm, and 2 mm. In the data evaluation the glass samples were assumed to be plane-parallel windows under perpendicular irradiation with a collimated beam. The phase boundary reflectivity was modelled with the Fresnel Eqs. (A.3). Absorption in the window's volume was modelled with Lambert Beer's law, Eq. (A.1). Ten window-internal reflections were considered. Scattering was neglected.

The refractive index of the 2 mM potassium ferrioxalate solution employed in the actinometry experiments was assumed to equal the refractive index of pure water and taken from literature [26]. The Napierian absorption coefficient of the 2 mM potassium ferrioxalate solution was derived from transmittance measurements of a sample in an optical quartz glass (QS) cuvette with an optical thickness of 10 mm using an Agilent 8453 UV–vis spectrometer, Fig. B.2A. The measurements were taken relative to a reference water sample in the same QS cuvette. The data evaluation was assuming perpendicular irradiation with a collimated beam, the optical path length being equal to the layer thickness of the cuvette and Lambert Beer's law (A.1) to model the ray attenuation.

The refractive index of the aerogel supported titania-based catalyst powder can be assumed to be close to the refractive index of air and therefore was set to unity in all simulations. The Napierian absorption and scattering coefficients were derived from diffuse reflectance and transmittance measurements of a powder sample in a Spectrosil® quartz glass cuvette (QS) with an optical thickness of 1 mm, Fig. B.2B. To prepare the catalyst sample, 10 mg of activated titania catalyst powder were mixed with 1 mL of aerogel support in a 5 mL borosilicate vessel with a snap on cap by rigorous shaking. The measurements were conducted with a Perkin Elmer Lambda 1050 UVVIS spectrometer equipped with an integrating sphere assembly. For precise measurements of the diffuse reflectance, the measurements were taken relative to a Zenith Polymer diffuse reflection standard from Sphere Optics GmbH and corrected accordingly. The powder sample was measured three times with random agitation of the cuvette between the repeat measurements to check influences of the random order of the aerogel and titania particles in the quartz glass cuvette on the derived transmittance and reflectance values. In the data evaluation the sample cell filled with catalyst powder was mapped in the MATLAB®-based Monte Carlo ray tracing simulation environment considering absorption and scattering in the catalyst bed volume and refraction and partial reflection on the phase boundaries between environment and glass and glass and catalyst bed. The incoming light was assumed to be perpendicular to the cuvette surface and ideally collimated.

From the onset of the determined absorption coefficient of the aerogel supported titania-based photocatalyst, in Fig. B.2B, the band gap can be estimated to lie at approx. 403 nm which equals 3.08 eV and is in good agreement with literature data for titania [27].

Appendix C. . Light source characterization

The total spectral photon emission of employed the LED light source modules was derived in goniometer measurements using a RIGO801-300 photogoniometer from TechnoTeam GmbH. The goniometer was equipped with a calibrated UV–vis spectrometer measuring the irradiance (E_λ) in positions on the spherical surface scanned by the goniometer arm. The spherical cap scanned in the measurement covers an azimuth angle (φ) from $0°$ to $360°$ (full round) and a polar angle (θ) from $0°$ (perpendicular view on the LED light source modules) to $110°$ and had a radius (r) equal to 310 mm. The step width in both azimuth and polar angle in the measurements was $5°$. From the irradiance data recorded in the roughly 3200 positions on the scanned spherical cap, the total spectral emission (q_λ) was calculated over a sphere surface integral, Eq. (C.1).

$$q_\lambda = \int E_\lambda dA = r^2 \int E_\lambda sin(\theta)d\theta d\varphi \tag{C.1}$$

To reduce the measurement time, the full scan of the sphere cap was only conducted for the highest of all LED drive current settings. The characteristic linking the LED drive current (I_{LED}) to the total emission of the LED light source modules was derived from irradiance measurements in one position ($\varphi = 180°$, $\theta = 0°$) and Eq. (C.2).

$$q_\lambda(I_{LED}) = q_\lambda(I_{LED,scan}) \frac{E_\lambda(I_{LED})}{E_\lambda(I_{LED,scan})} \tag{C.2}$$

For convenient data handling in the quantum yield evaluation in this contribution, the determined LED light source module emission spectra are normalized to their area and the LED characteristic expressed as relation between the LED drive current and the total emission power, Fig. C.1A and B. To yield the total emission spectrum at a specific drive current setting the total emission power read from the characteristic (Fig. C.1B) acts as linear scaling factor for the corresponding normalized total emission spectrum (Fig. C.1A) to yield the desired total emission spectrum at the specific drive current setting. The conversion of the energy-based data in Fig. C.1 to the photon number-based data required for the evaluations according to Eqs. (6) and (9) is executed with Eq. (C.3). Thereby h and ν correspond to the Planck constant and the frequency of photons at the specific wavelength, respectively.

$$q_{p,\lambda} = \frac{q_\lambda}{h\nu} \tag{C.3}$$

The measurement range of the employed UVVis spectrometer starts at 350 nm. However, data below 370 nm is noisy and likely inaccurate, pale spectra in the background Fig. C.1. To reduce the influence of this noise the spectra were fitted with a gaussian-like curve and the noisy end replaced by the fit data, solid spectra in the foreground Fig. C.1. However, the emission spectrum of the 365 nm LED light source module might significantly be influenced by the noise at the lower end of the measurement range of the employed spectrometer and therefore be less accurate.

The LED drive currents in goniometer measurements were generated by a high precision PTNhp 125–10 current source from Heinzinger electronic GmbH and measured with a LMG95 precision power meter from ZES ZIMMER Electronic Systems GmbH. The drive current settings were chosen to equal the drive current settings in the potassium ferrioxalate and methanol reforming experiments.

Appendix D. . Catalyst and catalyst support synthesis

Both the titania-based photocatalyst and the aerogel support powder were prepared in straight-forward literature reported synthesis routes prior to physically mixing them in the desired ratios.

To synthesize the titania catalyst with 0.025 wt-% palladium loading, commercial titania powder (AEROXIDE® TiO_2 P25, Evonik Industries) was loaded with palladium using an adapted wet-impregnation procedure prior to a calcination step [28,29]. 17.2 g titania were dispersed in 43 mL deionized water (DI, MilliQ) at 80 °C under continuous stirring. In a second beaker 10 mg palladium-(II)-nitrate hydrate ($Pd(NO_3)_2xH_2O$, ACROS Organics) was dissolved in 3 mL deionized water. Using a syringe, the palladium nitrate-solution was slowly dripped into the well mixed titania suspension under continuous stirring at 80 °C. The suspension was then further stirred and kept at 80 °C until it had a paste-like texture. To remove water residues, the paste was subsequently dried for 11 h at 110 °C (ramp of 5 K min^{-1}) under static air in an M110 muffle furnace from Thermo Scientific. Subsequently, the catalyst was calcined at 225 °C and a temperature ramp of 10 K min^{-1} for 3 h. The calcined catalyst was ground by hand using a mortar and sieved several times with an Analysette 3 PRO sieving machine from Fritsch GmbH to isolate catalyst particles with a size between 15 μm and 25 μm.

The silica aerogel serving as the catalyst support was synthesized separately according to a slightly modified standard sol gel procedure from literature [30]. 7.835 g of the silica precursor tetra methyl ortho silicate (TMOS, 99 %, ACROS Organics) was dissolved in 4.946 g of methanol (Methanol, technical grade greater than 99 %, Carl Roth GmbH und Co.KG) resulting in a molar ratio of TMOS to methanol of 1:3. In parallel, an ammonia solution was prepared by diluting 0.567 g of 25 wt-% ammonia solution in 150 g deionized water resulting in a molar ratio of ammonia to water of approx. 0.001:1. 3.723 g of the prepared water-ammonia solution was subsequently dripped in approx. 60 s into the TMOS methanol solution under constant rigorous stirring resulting in a TMOS to methanol to water to ammonia molar ratio of 1:3:4:0.004. Immediately after completed mixing, the reacting sol was poured into methanol wetted polytetrafluoroethylene (PTFE) moulds, that were covered with a watch glass until gelation occurred (~9 min at room temperature). Directly after the gelation, the gels were covered with plenty of methanol and aged for seven days. The methanol supernatant was exchanged after two and four days of aging. Lastly, the alcogel was dried in supercritical CO_2 with a continuous CO_2 flow of approx. 200 L_N/h at 120 bar and 60 °C for 20 h using an HPE-300 supercritical drier from EUROTECHNICA GmbH. Analogue to the active titania-based catalyst, the silica aerogel was ground using a mortar and sieved to obtain the desired particle size fraction of 100 to 200 μm resulting in a low-density translucent and fluent aerogel powder.

For the optical dilution of the catalyst, 4 mg of the prepared 0.025 wt-% palladium on titania catalyst with a particle size between 15 and 25 μm was combined in a 1 mL precision measuring cylinder with 0.4 mL of the aerogel powder with a particle size of 100 to 200 μm and mixed rigorously through intense shaking. The needed amount (~0.23 mL) aerogel catalyst mixture was then transferred into the reaction tube and held in place during the kinetic measurements with quartz wool plugs.

Prior to the kinetic measurements, the optically diluted catalyst system was activated for 3 h *in situ* in the reactor under 5 mL_N min^{-1} hydrogen flow at 10 bar rel. and a temperature of 260 °C. Heating/cooling rates in the activation interval were 5 K min^{-1}. To avoid high temperatures at the optics module during the activation procedure, the optics module and heating brackets in place can be moved without disassembly of the reactor. Thereby the heating brackets can be placed around the reaction volume while the temperature of the optics module is never higher than 100 °C. After the activation, the positions of optics module and heating brackets must be interchanged. To remove any hydrogen traces before the kinetic measurements, the whole test rig was purged with nitrogen in a pressure swing purge procedure.

Appendix E. Supplementary data

Supplementary data to this article can be found online at https://doi.org/10.1016/j.cej.2022.139204.

References

[1] T. Uekert, C.M. Pichler, T. Schubert, E. Reisner, Solar-driven reforming of solid waste for a sustainable future, Nat. Sustain. 4 (2021) 383–391, https://doi.org/10.1038/s41893-020-00650-x.

[2] D. Wang, M.A. Mueses, J.A.C. Márquez, F. Machuca-Martínez, I. Grčić, R. Peralta Muniz Moreira, G. Li Puma, Engineering and modeling perspectives on photocatalytic reactors for water treatment, Water Res. 202 (2021) 117421.

[3] A. Dutta, N. Das, D. Sarkar, S. Chakrabarti, Development and characterization of a continuous solar-collector-reactor for wastewater treatment by photo-Fenton process, Sol. Energy 177 (2019) 364–373, https://doi.org/10.1016/j.solener.2018.11.036.

[4] Ü. Taştan, D. Ziegenbalg, Photochlorination of toluene – the thin line between intensification and selectivity. Part 1: intensification and effect of operation conditions, React. Chem. Eng. 6 (2021) 82–89, https://doi.org/10.1039/D0RE00263A.

[5] H. Nishiyama, T. Yamada, M. Nakabayashi, Y. Maehara, M. Yamaguchi, Y. Kuromiya, Y. Nagatsuma, H. Tokudome, S. Akiyama, T. Watanabe, R. Narushima, S. Okunaka, N. Shibata, T. Takata, T. Hisatomi, K. Domen, Photocatalytic solar hydrogen production from water on a 100–m2 scale, Nature 598 (2021) 304–307, https://doi.org/10.1038/s41586-021-03907-3.

[6] R. Schäppi, D. Rutz, F. Dähler, A. Muroyama, P. Haueter, J. Lilliestam, A. Patt, P. Furler, A. Steinfeld, Drop-in Fuels from Sunlight and Air, Nature 601 (7891) (2022) 63–68.

[7] B.A. Pinaud, J.D. Benck, L.C. Seitz, A.J. Forman, Z. Chen, T.G. Deutsch, B.D. James, K.N. Baum, G.N. Baum, S. Ardo, H. Wang, E. Miller, T.F. Jaramillo, Technical and economic feasibility of centralized facilities for solar hydrogen production via photocatalysis and photoelectrochemistry, Energy Environ. Sci. 6 (2013) 1983, https://doi.org/10.1039/c3ee40831k.

[8] R.J. Braham, A.T. Harris, Review of Major Design and Scale-up Considerations for Solar Photocatalytic Reactors, Ind. Eng. Chem. Res. 48 (2009) 8890–8905, https://doi.org/10.1021/ie900859z.

[9] Q. Wang, C. Pornrungroj, S. Linley, E. Reisner, Strategies to improve light utilization in solar fuel synthesis, Nat. Energy 7 (2022) 13–24, https://doi.org/10.1038/s41560-021-00919-1.

[10] S.E. Braslavsky, A.M. Braun, A.E. Cassano, A.V. Emeline, M.I. Litter, L. Palmisano, V.N. Parmon, N. Serpone, Glossary of terms used in photocatalysis and radiation catalysis (IUPAC Recommendations 2011), Pure Appl. Chem. 83 (2011) 931–1014, https://doi.org/10.1351/PAC-REC-09-09-36.

[11] Q. Wang, T. Hisatomi, Q. Jia, H. Tokudome, M. Zhong, C. Wang, Z. Pan, T. Takata, M. Nakabayashi, N. Shibata, Y. Li, I.D. Sharp, A. Kudo, T. Yamada, K. Domen, Scalable water splitting on particulate photocatalyst sheets with a solar-to-

hydrogen energy conversion efficiency exceeding 1, Nat. Mater. 15 (2016) 611–615, https://doi.org/10.1038/nmat4589.

[12] F. Dionigi, P.C.K. Vesborg, T. Pedersen, O. Hansen, S. Dahl, A. Xiong, K. Maeda, K. Domen, I. Chorkendorff, Gas phase photocatalytic water splitting with Rh2−yCryO3/GaN:ZnO in micro-reactors, Energy Environ. Sci. 4 (2011) 2937, https://doi.org/10.1039/c1ee01242h.

[13] Y. Sakata, T. Hayashi, R. Yasunaga, N. Yanaga, H. Imamura, Remarkably high apparent quantum yield of the overall photocatalytic H2O splitting achieved by utilizing Zn ion added Ga2O3 prepared using dilute CaCl2 solution, Chem. Commun. (Camb.) 51 (2015) 12935–12938, https://doi.org/10.1039/C5CC03483C.

[14] T. Takata, J. Jiang, Y. Sakata, M. Nakabayashi, N. Shibata, V. Nandal, K. Seki, T. Hisatomi, K. Domen, Photocatalytic water splitting with a quantum efficiency of almost unity, Nature 581 (2020) 411–414, https://doi.org/10.1038/s41586-020-2278-9.

[15] A.V. Emeline, X. Zhang, M. Jin, T. Murakami, A. Fujishima, Application of a "black body" like reactor for measurements of quantum yields of photochemical reactions in heterogeneous systems, J. Phys. Chem. B 110 (2006) 7409–7413, https://doi.org/10.1021/jp057115f.

[16] H.J. Kuhn, S.E. Braslavsky, R. Schmidt, Chemical actinometry (IUPAC Technical Report), Pure Appl. Chem. 76 (2004) 2105–2146, https://doi.org/10.1351/pac200476122105.

[17] C.G. Hatchard, C.A. Parker, A new sensitive chemical actinometer - II. Potassium ferrioxalate as a standard chemical actinometer, Proc. R. Soc. Lond. A 235 (1956) 518–536, https://doi.org/10.1098/rspa.1956.0102.

[18] B. Wriedt, D. Ziegenbalg, Common pitfalls in chemical actinometry, J Flow Chem 10 (2020) 295–306, https://doi.org/10.1007/s41981-019-00072-7.

[19] B. Wriedt, D. Ziegenbalg, Application Limits of the Ferrioxalate Actinometer**, ChemPhotoChem 5 (10) (2021) 947–956.

[20] T. Lehóczki, É. Józsa, K. Ősz, Ferrioxalate actinometry with online spectrophotometric detection, J. Photochem. Photobiol., A 251 (2013) 63–68, https://doi.org/10.1016/j.jphotochem.2012.10.005.

[21] S. Escobedo Salas, B. Serrano Rosales, H. de Lasa, Quantum yield with platinum modified TiO2 photocatalyst for hydrogen production, Applied Catalysis B: Environmental 140–141 (2013) 523–536, https://doi.org/10.1016/j.apcatb.2013.04.016.

[22] M.P. Languer, F.R. Scheffer, A.F. Feil, D.L. Baptista, P. Migowski, G.J. Machado, D. P. de Moraes, J. Dupont, S.R. Teixeira, D.E. Weibel, Photo-induced reforming of alcohols with improved hydrogen apparent quantum yield on TiO2 nanotubes loaded with ultra-small Pt nanoparticles, Int. J. Hydrogen Energy 38 (2013) 14440–14450, https://doi.org/10.1016/j.ijhydene.2013.09.018.

[23] O. Fontelles-Carceller, M.J. Muñoz-Batista, J.C. Conesa, M. Fernández-García, A. Kubacka, UV and visible hydrogen photo-production using Pt promoted Nb-doped TiO 2 photo-catalysts: Interpreting quantum efficiency, Appl. Catal. B 216 (2017) 133–145, https://doi.org/10.1016/j.apcatb.2017.05.022.

[24] O. Fontelles-Carceller, M.J. Muñoz-Batista, E. Rodríguez-Castellón, J.C. Conesa, M. Fernández-García, A. Kubacka, Measuring and interpreting quantum efficiency for hydrogen photo-production using Pt-titania catalysts, J. Catal. 347 (2017) 157–169, https://doi.org/10.1016/j.jcat.2017.01.012.

[25] M. Montalti, A. Credi, L. Prodi, M.T. Gandolfi, J. Michl, V. Balzani, Handbook of photochemistry, Third edition, CRC/Taylor & Francis, Boca Raton, 2020.

[26] G.M. Hale, M.R. Querry, Optical Constants of Water in the 200-nm to 200-mum Wavelength Region, Appl. Opt. 12 (1973) 555, https://doi.org/10.1364/AO.12.000555.

[27] D. Reyes-Coronado, G. Rodríguez-Gattorno, M.E. Espinosa-Pesqueira, C. Cab, R. de Coss, G. Oskam, Phase-pure TiO(2) nanoparticles: anatase, brookite and rutile, Nanotechnology 19 (14) (2008) 145605.

[28] M. Selinsek, B.J. Deschner, D.E. Doronkin, T.L. Sheppard, J.-D. Grunwaldt, R. Dittmeyer, Revealing the Structure and Mechanism of Palladium during Direct Synthesis of Hydrogen Peroxide in Continuous Flow Using Operando Spectroscopy, ACS Catal. 8 (2018) 2546–2557, https://doi.org/10.1021/acscatal.7b03514.

[29] T. Inoue, M.A. Schmidt, K.F. Jensen, Microfabricated Multiphase Reactors for the Direct Synthesis of Hydrogen Peroxide from Hydrogen and Oxygen, Ind. Eng. Chem. Res. 46 (2007) 1153–1160, https://doi.org/10.1021/ie061277w.

[30] L.M. Sanz-Moral, M. Rueda, R. Mato, Á. Martín, View cell investigation of silica aerogels during supercritical drying: Analysis of size variation and mass transfer mechanisms, J. Supercritical Fluids 92 (2014) 24–30, https://doi.org/10.1016/j.supflu.2014.05.004.

[31] Paul Kant, phoRex & QY photoreactor - Monte Carlo ray tracing in MATLAB & quantum yield measurements, KITopenData (2022), https://doi.org/10.5445/IR/1000150817.